Gil-Santos, A.; Szakacs, G.; Moelans, N.; Hort, N.; van der Biest, O.:
Microstructure and mechanical characterization of cast Mg-Ca-Si alloys
In: Journal of Alloys and Compounds (2016) Elsevier

DOI: 10.1016/j.jallcom.2016.10.059

Microstructure and mechanical characterization of cast Mg-Ca-Si alloys

Andrea Gil-Santos[1], Gabor Szakacs[2], Nele Moelans[1], Norbert Hort[2], Omer Van der Biest[1]

[1]Department of Materials Engineering, KU Leuven, Kasteelpark Arenberg, 44, 3001 Leuven, Belgium
[2]Magnesium Innovation Centre (MagIC), Helmholtz-Zentrum Geesthacht, Max-Planck-Strasse 1, 21502 Geesthacht, Germany

e-mail corresponding author: andrea.gilsantos@mtm.kuleuven.be, andrea.gil.santos@hotmail.com

Abstract

Three different phase fields are predicted and experimentally detected in the Mg rich corner of the Mg-Ca-Si ternary diagram. The present phases are Mg + MgCaSi + Mg_2Si in phase field 1, Mg + MgCaSi in phase field 2 and Mg + Mg_2Ca + MgCaSi in phase field 3. The focus of this study is on the formation and evolution of the intermetallic phases. The final microstructures have been related with their solidification process and with the alloys mechanical properties. A clear influence of the observed intermetallic phases on the mechanical performance was found. A bigger size and higher amounts of the MgCaSi intermetallic phase increase the alloys strength and make them brittle, while in its fine morphology MgCaSi reduces the strengthening effect and slightly decreases the ductility compared to pure Mg. Mg_2Si phase in its needle-like small size morphology contributes to an increase of the hardness and compressive strength. Its presence reduces the alloys ductility making them brittle. Finally, the highest values for compressive strength and hardness are related to the Mg_2Ca presence.

Keywords: Intermetallics; rapid-solidification; mechanical properties; microstructure.

1. Introduction

This study is investigating a novel magnesium alloy system with the aim of getting a new resorbable material for biomedical applications. Calcium and silicon were selected as alloying elements due to their biocompatibility with the human body. Therefore, the microstructure and mechanical properties of cast ternary Mg-Ca-Si alloys have been studied as a function of alloy composition. The alloys were initially modelled by thermodynamic calculations and subsequently processed by casting, which allows a comparative study between the predicted and the experimentally obtained phase compositions.

Magnesium and its alloys are nowadays investigated worldwide for biomedical applications [1, 2]. Mg is known for its good biocompability and bioactivity and Ca and Si, which are naturally in the human body, [2, 3] are involved in essential body functions and necessary for the bone regeneration processes [4]. The human adult body contains about 1100g of Ca, nearly 1.5% of the body weight, and 99% of this Ca is contained in the skeleton. Ca is an indispensable macroelement that performs essential

functions in bone structures [4]. Also Si has an essential role in bone formation as silicon ions are involved in the calcification process of young bones [5, 6]. Mg-Ca-Si alloys are thus suitable candidates for implant components with a minimized risk of rejection and toxicity.

Apart from their function in the body, Ca and Si can improve the mechanical properties of Mg-based alloys and facilitate their production process. The low solubility of Ca in Mg results in the formation of the intermetallic phase Mg_2Ca. When located at grain boundaries, this compound can result in grain refinement of the Mg matrix. Si has a lower solubility in Mg (0.006wt.%). A very small addition of Si into Mg results in a pronounced increase in ductility, while the tensile strength remains almost unaffected. For larger amounts of Si, the hardness and the tensile strength are improved by the presence of small Mg_2Si precipitates (<2μm) [7]. Si is known to increase the fluidity of the melt [8], which is important for casting.

The Mg rich corner of the ternary Mg-Ca-Si system has rarely been studied in as cast conditions [9-11]. In the reported investigations a post casting treatment is applied (heat treatment, extrusion…). However the final microstructure and mechanical properties of cast alloys strongly depend on the solidification process. Some of the final material characteristics will always be related to the initial cast conditions, regardless of the post casting treatment. Therefore, further understanding of the phase formation during solidification is essential.

In order to study the solidification sequence, thermodynamic calculations were performed that predict the phase formation process. The calculations are based on two different models. The first one is the equilibrium model, where solidification takes place throughout equilibrium states. The second is the Scheil or non-equilibrium model, where fast solidification is considered.

In this study, 9 alloys in the Mg rich corner were produced and characterized by identifying the present intermetallic phases in each region. The observed phases have been compared with the predicted phase assembly. Furthermore, the fraction of solid phases and the sequence of solid phase formation have been estimated from the samples and compared with the theoretical predictions. Finally, the influence of the intermetallic compounds on the mechanical properties has been analyzed.

2. Experimental procedure

The samples were processed by permanent mould gravity casting. Raw materials consisted of pure Mg (99.9 %), Si (99.9 %) and Ca chips (97.3 %). An electrical resistance furnace was used to melt the alloys under a protective atmosphere of Ar and SF_6. Mg was molten at 700°C and the Si and Ca chips, pre-heated at 400°C, were added to the melt. The alloys were kept for 45 min at 700-750°C before stabilization at 760°C and then poured into a 400°C preheated steel mould. Hexagonal BN was used as a mould release agent. The alloys were cooled down to room temperature (RT) in air.

The compositions of the alloys produced and studied in this work and the major impurities detected in the samples after casting are included in Table 1.

Table I. Compositions and trace elements of the cast Mg-Ca-Si alloys (wt.%) analysed by ICP-OES.

Sample name	Composition in wt.%	Ratio Ca:Si	Trace elements in wt.% *					
			Al	Cu	Fe	Mn	Ni	Total
A	Mg 0.19Ca 0.25Si	0.76	0.009	0.005	0.008	0.005	0.006	0.03
B	Mg 0.52Ca 0.50Si	1.04	0.005	0.001	0.032	0.006	0.001	0.05
C	Mg 0.50Ca 0.55Si	0.91	0.033	0.002	0.008	0.004	0.001	0.05
D	Mg 0.29Ca 0.19Si	1.53	0.003	0.001	0.024	0.016	0.001	0.04
E	Mg 0.18Ca 0.15Si	1.20	0.007	0.001	0.011	0.003	0.001	0.02
F	Mg 0.20Ca 0.15Si	1.33	0.004	0.001	0.018	0.007	0.001	0.03
G	Mg 1.34Ca 0.41Si	3.27	0.010	0.001	0.011	0.005	0.001	0.03
H	Mg 1.43Ca 0.16Si	8.94	0.015	0.001	0.005	0.006	0.001	0.03
I	Mg 1.70Ca 0.10Si	17.00	0.010	0.001	0.006	0.007	0.001	0.02

* The amount of trace elements is given here for the sake of completeness. We assume however that their amounts are so small that they do not affect the results. The effect of these traces is therefore not considered in the further discussion in this paper.

Disk shaped specimens with a thickness of 2 mm were cut from the cast rod for microstructural characterization. They were ground and polished with alumina suspension and water-free colloidal silica solution. Since burn-off takes place during preparation (evaporation, oxidation, etc) the compositions and impurities after solidification were measured by a Varian 720 ES inductively coupled plasma optical emission spectrometer (ICP-OES). Microstructure analysis was carried out using an optical microscope and a Philips XL30 FEI scanning electron microscope (SEM) equipped with an EDAX TSL energy dispersive X-ray spectroscopy (EDS) detector. Optical micrographs were taken after etching the surface in order to easily reveal the microstructure. The etching agent used was picric acid based, containing 10 mL of acetic acid, 4.2 g of picric acid, 20 mL H_2O and 50 mL ethanol. The average grain size was measured using Image-Pro Plus 6.0 software on images from the etched surfaces, using the linear intercept method according to the standard ASTM: E112-13 (2013) [12]. Optical micrographs and micrographs taken under polarized light revealed the grain boundaries with a similar quality.

The identification of secondary phases in the alloys was carried out by X-ray diffraction (XRD) using a Seifert 3003-TT. Cu-Kα radiation was used at 40 kV and 40 mA. A two theta scan was performed from 20° to 80° with a 0.02° step size. The phase identification was done by comparison using the Pearson database. Due to the small amount of secondary phases the identification was combined with field emission electron probe microanalysis (EPMA) in a FEG EPMA JXA-5830F. The phase identification was always performed on as-cast samples at room temperature. The phase volume fractions were measured from the micrographs using the Image-J software.

Cylindrical compression test samples (6 mm diameter and 10 mm height) were machined from the cast samples by electric discharge machining (EDM). The compression tests were performed at room temperature on an Instron 4600, applying the load parallel to the axis of the cast cylinder at a constant speed of 0.5 mm/min. The Vickers hardness of the alloys was measured using a Leitz durometer under 25 grams load. The microhardness tester was equipped with a diamond tip shaped in a 136° square-based pyramid and 15 measurements were taken per sample.

Thermodynamic calculations were performed using Thermo-Calc 2015b [13] software with the commercial Mg database TCMG2. During solidification, diffusion in the solid phase is often limited compared to the diffusion in the liquid. In order to interpret the phase formation during the solidification two extreme cases were therefore applied, namely the equilibrium and the Scheil or non-equilibrium modes [14]. In equilibrium infinitely fast diffusion is considered for both liquid and solid phase while under Scheil condition the diffusion in liquid is assumed to be infinitely fast [15, 16] while that in solid phases is negligible [17].

3. Results and Discussion

3.1 Thermodynamic calculations

Despite the very different assumptions, the final phase fractions of the solid phases obtained in the Scheil and equilibrium solidification simulations were very similar for the considered alloys. The results are presented in Table II.

Table II. Predicted vs. experimental phase fraction (wt.%) at 300°C for the considered alloys in the three different phase fields.

Phase field	**Sample composition (wt.%)**	Predicted phases (wt.%)						Experimental phases(wt.%)		
		Mg_2Ca		**MgCaSi**		**Mg_2Si**		**Mg_2Ca**	**MgCaSi**	**Mg_2Si**
		Scheil	Equilibrium	Scheil	Equilibrium	Scheil	Equilibrium			
1	A. Mg 0.19Ca 0.25Si			0.34	0.31	0.34	0.34		0.2 ± 0.1	0.3 ± 0.1
Mg + Mg_2Si + MgCaSi	B. Mg 0.52Ca 0.50Si			0.54	0.55	0.36	0.39		0.6 ± 0.2	1.0 ± 0.2
	C. Mg 0.50Ca 0.55Si			1.14	1.15	0.50	0.57		1.2 ± 0.2	2.8 ± 0.2
2	D. Mg 0.29Ca 0.19Si			0.62	0.45	0.00	0.00		2.3 ± 0.3	
Mg + MgCaSi	E. Mg 0.18Ca 0.15Si			0.40	0.44	0.06	0.07		1.6 ± 0.3	
	F. Mg 0.20Ca 0.15Si			0.45	0.41	0.00	0.04		0.9 ± 0.2	
3	G. Mg 1.34Ca 0.41Si	1.49	1.47	1.35	1.45			0.8 ± 0.2	2.8 ± 0.4	
Mg + Mg_2Ca + MgCaSi	H. Mg 1.43Ca 0.16Si	2.42	2.57	0.53	0.54			4.4 ± 0.5	0.6 ± 0.2	
	I. Mg 1.70Ca 0.10Si	3.16	3.39	0.33	0.35			3.9 ± 0.4	0.4 ± 0.1	

An overview of the Mg-Ca-Si isothermal section at 300°C is shown in Figure 1a and the enlarged Mg rich corner including the studied compositions is presented in Figure 1b. Three different phase fields arise in the Mg rich corner. The phases are Mg + MgCaSi + Mg_2Si in phase field 1, Mg + MgCaSi in phase field 2 and Mg + Mg_2Ca + MgCaSi in phase field 3.

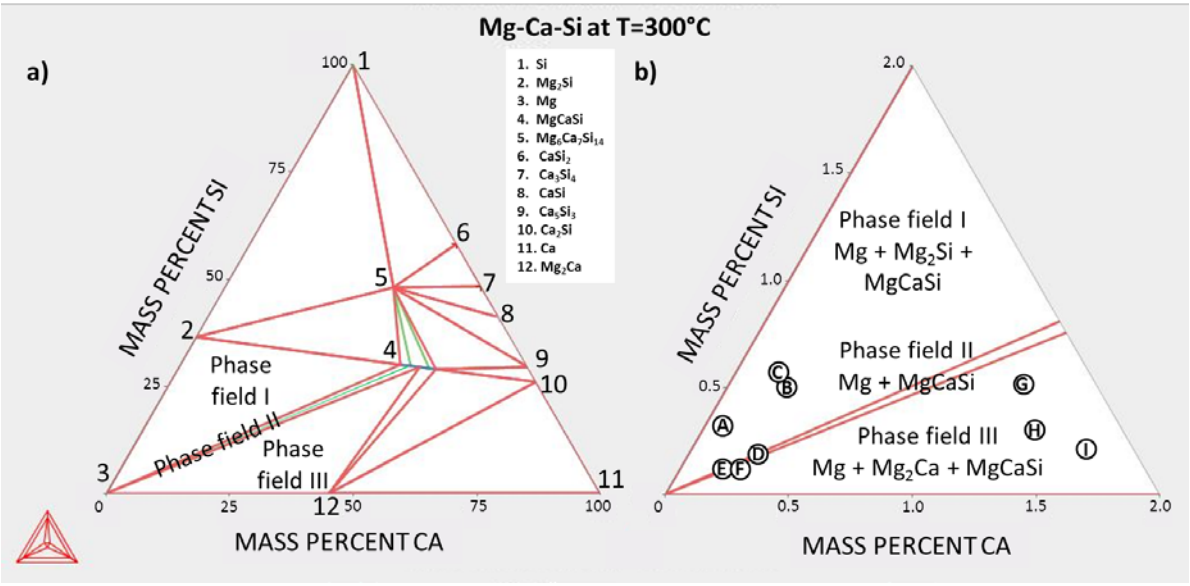

Figure 1. a) Mg-Ca-Si isothermal section at 300°C showing the different phase fields (wt.%) and b) a closer view on the Mg-rich corner including the investigated compositions (A-I).

The phase formation temperatures obtained under equilibrium and Scheil calculations are summarized in Table III. Important to notice is that the primary solidifying phase depends on the alloy composition. Mg is the first phase forming in alloys A, D, E and F while for the other alloys MgCaSi is the primary phase. The temperature gap between the formation of the different phases is also changing with composition which affects the final microstructure. This knowledge helps to explain the size of the observed intermetallics in the alloys. Both equilibrium and non-equilibrium calculations predicted the same primary phases and similar phase formation temperatures.

Table III. Comparison between the phase formation temperatures calculated under equilibrium and non-equilibrium (Scheil) conditions. Underlined temperatures correspond to the primary solidifying phase for the given composition.

Phase field	**Sample composition (wt.%)**	**Estimated temperature formation (°C)**							
		Mg		**MgCaSi**		**Mg_2Ca**		**Mg_2Si**	
		Scheil	Equilibrium	Scheil	Equilibrium	Scheil	Equilibrium	Scheil	Equilibrium
1	A. Mg0.19Ca0.25Si	<u>647</u>	<u>647</u>	644	644			637	637
	B. Mg 0.52Ca 0.50Si	644	645	<u>660</u>	<u>659</u>			637	637
	C. Mg 0.50Ca 0.55Si	644	645	<u>663</u>	<u>664</u>			637	637
2	D. Mg 0.29Ca 0.19Si	<u>647</u>	<u>647</u>	645	645			--	--
	E. Mg 0.18Ca 0.15Si	<u>648</u>	<u>648</u>	645	645			637	637
	F. Mg 0.20Ca 0.15Si	<u>648</u>	<u>648</u>	645	645			--	637
3	G. Mg 1.34Ca 0.41Si	643	643	<u>703</u>	<u>703</u>	518	519		
	H. Mg 1.43Ca 0.16Si	642	643	<u>656</u>	<u>656</u>	518	519		
	I. Mg 1.70Ca 0.10Si	640	640	<u>642</u>	<u>643</u>	518	519		

3.2 Experimental microstructures and phase identification

The three phase fields in the Mg-rich corner (Figure 1) can be distinguished by the intermetallic phases that co-exist with Mg. This differentiation is included in the first column of Table II. The phase identification is presented in Figure 2. The microstructures, phase compositions and thermodynamic predictions are compared separately below by different phase fields.

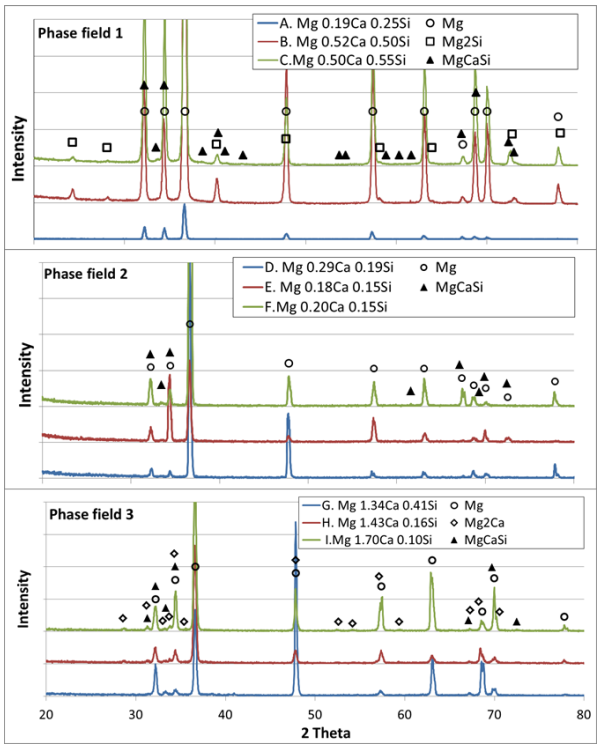

Figure 2. XRD patterns and phase identification of alloys from the three different phase fields.

3.2.1. <u>Phase field 1</u> : Mg + Mg_2Si + MgCaSi

The intermetallic phases observed in the samples A to C are Mg_2Si and MgCaSi (Figure 3 a, b and c). The ternary MgCaSi looks white and bright in the BSE micrographs while the binary Mg_2Si has a light grey tone.

MgCaSi appears in alloys A and B in its fine needle-like shape (1.0-5.0 µm length and 0.5 µm width). In alloy C it appears in the form of polygons with linear etches and the particles have a bigger size (2.5 µm length and width). The increase of both Si and Ca concentration from alloy A (0.44wt.%) to B (1.02 wt.%) and C (1.05 wt.%) results in the formation of bigger size particles of MgCaSi phase. The other intermetallic phase, Mg_2Si, is always observed in its needle-like shape, but thinner and smaller than the fine MgCaSi phase. Mg_2Si appears forming clusters of the compound. In alloy C the cluster formation is more evident since the total amount of Mg_2Si is higher than in alloys A or B. A higher amount of Si in the alloy composition produces a higher amount of Mg_2Si phase in the microstructure (Table II) but its morphology does not change.

In alloys B and C (Figure 3 b and c), the MgCaSi compound appears surrounded mainly by Mg that separates them from the Mg_2Si. It suggests that MgCaSi is a primary phase here, taking Ca and Si

from the liquid, resulting in a Mg rich area around the precipitates. In alloy A this phenomena is not observed and both intermetallics mingle in the microstructure. This change in microstructure with alloy composition is connected to the solidification process. From Table III in alloys B and C the first phase forming is MgCaSi (at 659°C and 664°C respectively) followed by Mg (at 645°C) and Mg_2Si (at 637°C). On the other hand, in alloy A, the sequence of phase formation is different. Mg forms first (at 647°C) and MgCaSi appears later as a secondary phase with less Mg available for its formation. This effect results in small MgCaSi particles located predominantly at the grain boundaries and their surroundings (as it was observed in Figure 3d).

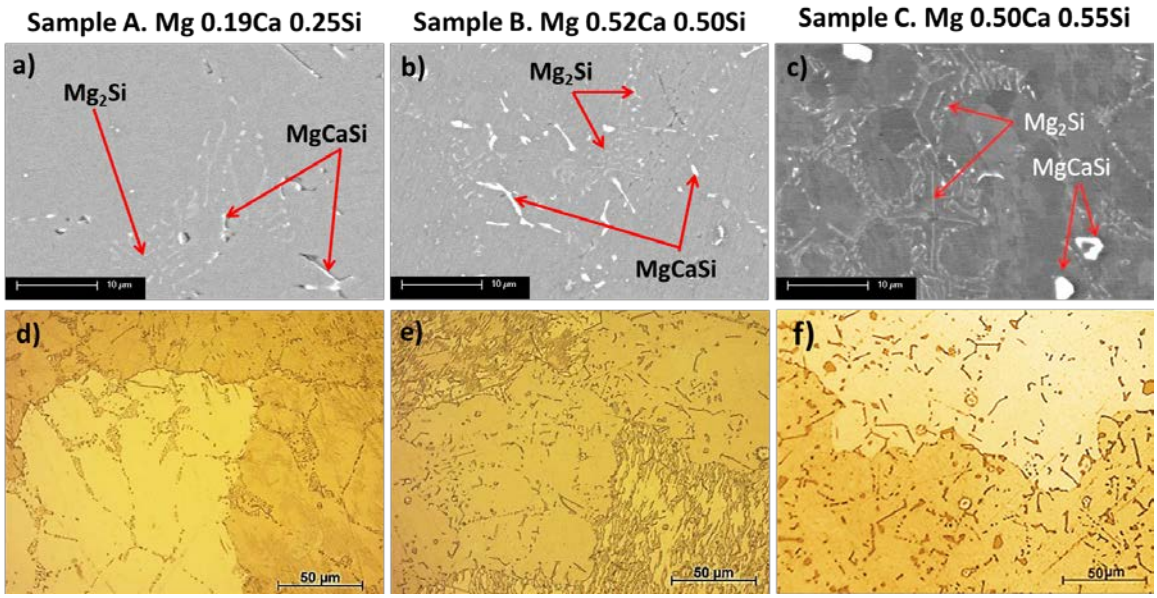

Figure 3. Identification in a, b and c of the phases Mg_2Si and MgCaSi in SEM images for samples in phase field 1. Images d, e and f from optical microscope of etched surfaces from same samples, the intermetallic phases appear darker in contrast to the Mg matrix and grains appear in different colors.

The average grain size is summarized in Table IV. Sample C has the largest grain size compared to A and B. In samples A and B, the MgCaSi particles are smaller and more homogeneously distributed than in sample C (Figure 3 a, b and c). Moreover, for compositions A and B, more MgCaSi particles are located at the grain boundaries and will act as barriers for grain growth, promoting grain refinement. When the ternary phase appears in its coarse morphology, as it does in alloy C, the grains grow bigger.

When comparing the predicted and experimental phase fractions (Table II) it can be conclude that the predictions in this region are in good qualitative agreement with the experiments. The predicted phases are experimentally observed and the changes with composition show similar trends in the simulations and experiments. The fraction of precipitated phases increases with the amount of Ca and Si added to the Mg.

The phase forming temperatures for the different phases under both equilibrium and Scheil conditions are compared in Table III. Since the differences between the values obtained with these two approaches are negligible, it can be concluded that for these alloys the equilibrium condition can be used as a reference and related with the real solidification.

3.2.2. Phase field 2 : Mg + MgCaSi

Figures 4 a, b and c show the microstructures for the alloy compositions in phase field 2. MgCaSi precipitates are distinguished thanks to their brighter colour compared to the grey background characteristic for Mg. In this field the MgCaSi morphology does not vary with composition and it forms in a fine needle-like shape. The lack of bigger particles suggests that Mg and MgCaSi start to solidify simultaneously, such that the ternary compound does not have the time to grow freely in the liquid.

The MgCaSi intermetallic is located along the grain boundaries and inside the grains (Figure 4 d, e and f). In this case the higher amount of MgCaSi phase does not lead to grain refinement as it did in phase field 1 since here the intermetallic precipitates are not necessarily located at the grain boundaries. In fact, the amount of MgCaSi decreases from sample D to F and the grain size (Table IV) decreases as well from sample D to F. When the amount of the ternary phase increases, the precipitates are mainly located inside the grains and it does not lead to an increased pinning effect of the precipitates or to an increased number of nucleation sites.

As in the previous case, the amount of MgCaSi increases with the Ca and Si content in the alloys (Table II). The amount of the ternary MgCaSi phase is higher in alloy D (2.3wt.%) than in E and F (1.6 wt.% and 0.9 wt.% respectively). The total amount of alloying elements evolves in the same way, it is higher in D (0.48 wt.%) and lower in both E and F (0.33 wt.% and 0.35 wt.% respectively).

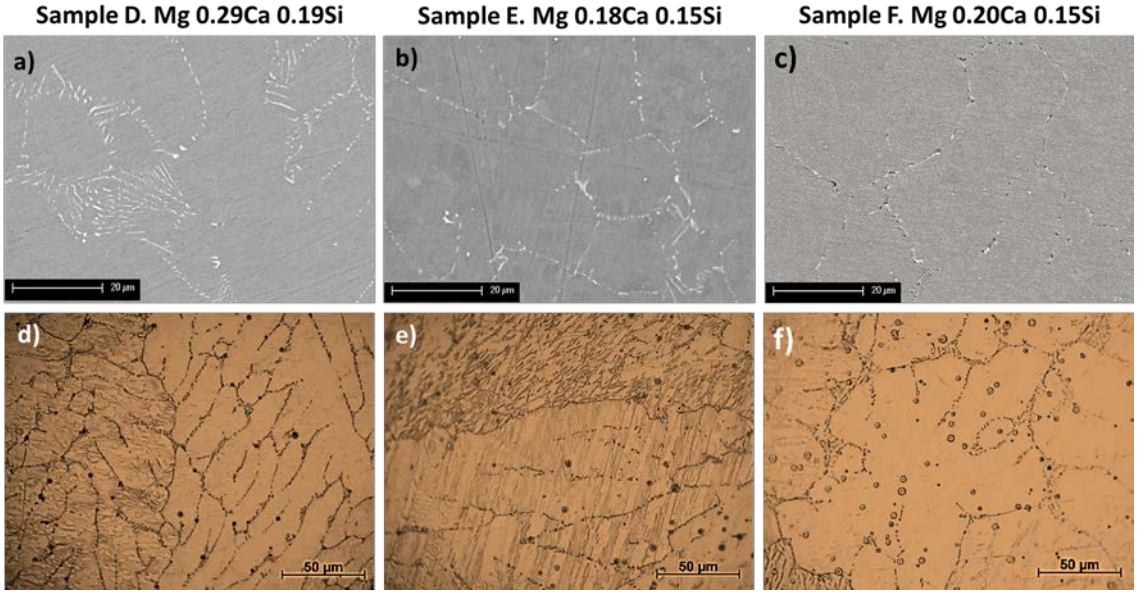

Figure 4. a, b and c: SEM micrographs of the samples D, E and F. The white phase is in all cases MgCaSi. The optical microscope pictures d, e and f show the grain boundaries and the MgCaSi phase located in grain boundaries and inside grains after etching the sample surfaces. Intermetallic phases appear darker in contrast with the Mg matrix. The intermetallic phases are all the darker marks within the grey matrix.

The results comparing the predicted and the experimentally measured phase fractions in phase field 2 are summarized in Table II. Predictions in this field are not always in qualitative agreement with the experiments. The MgCaSi predicted phase is the only one observed in the alloys but for alloys E and F, the Mg_2Si phase is also predicted under equilibrium conditions. Even if the expected amounts are

low (0.07 wt.% for alloy E and 0.04wt.% for F), it indicates a deviation between the equilibrium and the real solidification. Under Scheil conditions, Mg_2Si phase is only expected in a low percentage in alloy E (0.07 wt.%) but it is not predicted for alloy F. In this case Scheil conditions thus provide more realistic results than equilibrium. In all cases the witnessed microstructures show the two phases (Mg and MgCaSi) forming together, while it is not predicted from simulations. Also the amount of the predicted MgCaSi phase is about five times smaller than the experimentally observed. It can be concluded that the simultaneous formation of Mg and MgCaSi expected from alloy D is in fact happening as well in E and F.

When discerning the temperatures for phase formation in Table III, the primary phase is in all cases Mg, but there is only a difference of 2 or 3 degrees with the solidification temperature of the MgCaSi phase and we can thus conclude that in reality both phases form almost simultaneously, which is also clear from the experimental microstructures of alloys D, E and F.

The comparison of the equilibrium and Scheil forming temperatures (Table III) shows that there is no difference for the Mg and the MgCaSi phase, but there is for the Mg_2Si, and the Scheil predictions give more accurate values than the equilibrium. Nevertheless, in this case the absence of the Mg_2Si phase in alloys E and F could have been deduced from the equilibrium calculations as well. From them, the temperature at which the solid fraction reaches 100% can be obtained, being 636.86°C. The formation temperature of Mg_2Si is 636.90°C, which is only 0.02°C higher than the lowest solidification temperature. It is then clear that this phase did not have the chance to form during solidification.

3.2.3. Phase field 3 : Mg + Mg_2Ca + MgCaSi

The microstructures of the alloys in phase region 3 are presented in Figure 5 (a, b and c). The Mg_2Ca binary phase can be distinguished by its light grey colour and its round shape. The MgCaSi precipitates present a brighter tone and have a polygonal or needle-like shape.

The Mg_2Ca phase forms elongated and connected interdendritic films in alloys H and I (Figure 5 b and c) while in G the phase is present in a smaller amount and as isolated interdendritic particles (Figure 5a). This is a consequence of its volume fraction reduction in alloy G where its amount is smaller than 1 wt.% (Table II). It is also noticed that a higher concentration of Ca (and of Mg_2Ca) in alloy I leads to a highly connected network of Mg_2Ca along the grain boundaries than in H.

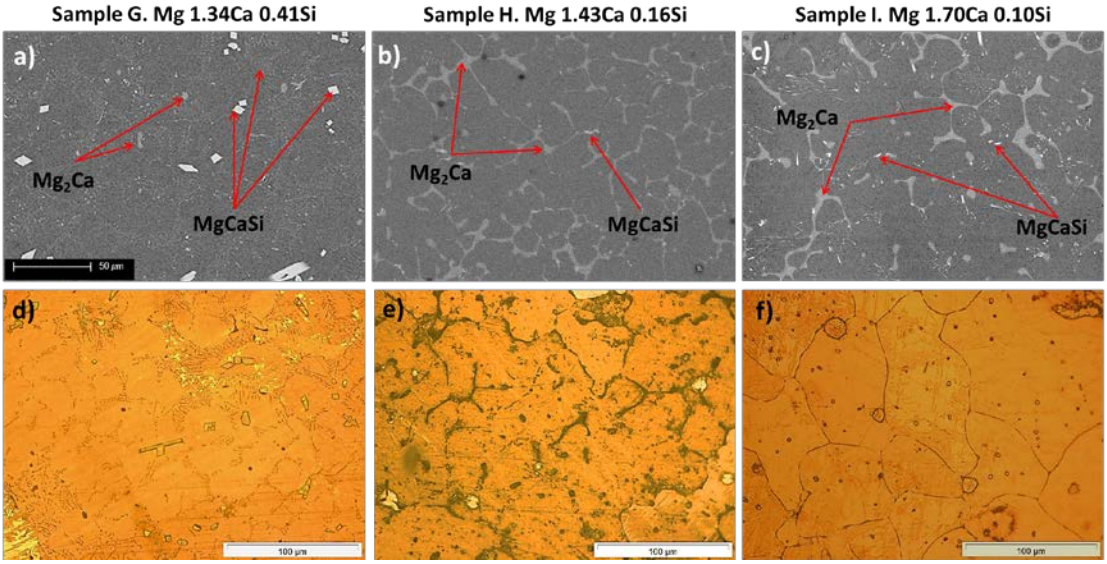

Figure 5. Identification of the phases in SEM images a, b and c for samples G, H and I. Images d, e and f from optical microscope of etched surfaces showing the grains.

The morphology of the ternary phase MgCaSi in G (Figure 5a) appears in the form of both coarse polygonal particles and fine needle-like ones. Nevertheless, in alloys H and I (Figure 5 b and c) it is only present in its needle-like shape and is more homogeneously distributed. The larger amount of MgCaSi in G (2.8wt.%) allows the precipitation of coarse particles while the smaller amount in H and I (0.6 and 0.4wt.%) results in finely distributed precipitates. The higher amount of MgCaSi phase is related to a higher Si content, namely 0.41wt.% Si in sample G and only 0.16 wt.% and 0.10 wt.% in samples H and I (Table II). When more Si is present , it reacts with Ca and Mg from the melt producing more MgCaSi. Less Ca is then available to form Mg_2Ca.That is the reason why only 0.8 wt.% of Mg_2Ca phase is observed in sample G versus the 4.4 and 3.9 wt.% in alloys H and I. In alloy G, MgCaSi coarse particles and fine MgCaSi are located in grain boundaries as well as regularly dispersed inside the grains. This can be more clearly observed in its etched surface (Figure 5 d) where intermetallic particles appear as darker spots in case of fine MgCaSi and elongated or square ones in case of coarse MgCaSi.

The grain sizes are included in Table IV. It is observed that the average grain size reduces with the amount of intermetallic phases. It seems that a higher ratio of wt.%Ca:wt.%Si results in a finer grain size. This higher ratio is also connected with a higher amount of Mg_2Ca phase in the specimens. Both intermetallics Mg_2Ca and MgCaSi can form in the grain boundaries (and inside the grains) but only Mg_2Ca contributes to the grain refinement effect.

The results comparing the predicted and experimentally measured phase fractions are summarized in Table II. Predictions in this field are in qualitative agreement with the experiments but some quantitative differences are still observed.

The results for the phase forming temperatures under equilibrium and Scheil conditions from Table III show no differences for this phase field; both phase formation temperatures can be used in solidification sequence predictions. The coarser MgCaSi particles present in alloy G that make its microstructure different from that in samples H and I can be linked to the solidification process. In all the alloys the primary crystallizing phase is the ternary MgCaSi (Table III). Afterwards the Mg starts

solidifying and finally the Mg_2Ca phase will form. In alloys H and I, the temperature gap between the formation of the ternary phase and the Mg phase is merely 15°C and 2°C, whereas in alloy G this temperature gap is substantially larger, 59°C, allowing the primary phase to grow freely and extensively in the melt. These predictions correspond with the observed bigger shape and size of the primary MgCaSi phase for alloy G (Figure 5a).

3.3 Mechanical behaviour

The relation between microstructures and mechanical behaviour can be analyzed considering the hardness values (Figure 6), the compression test data (Figure 7 and Table IV), and the described microstructures.

Figure 6 summarizes the hardness values obtained for the cast Mg-Ca-Si alloys. The positive effect of particles (especially Mg_2Si and Mg_2Ca) on hardness is clear. Even those with a grain size higher than that for pure Mg (A, C, D and E), are harder than pure Mg.

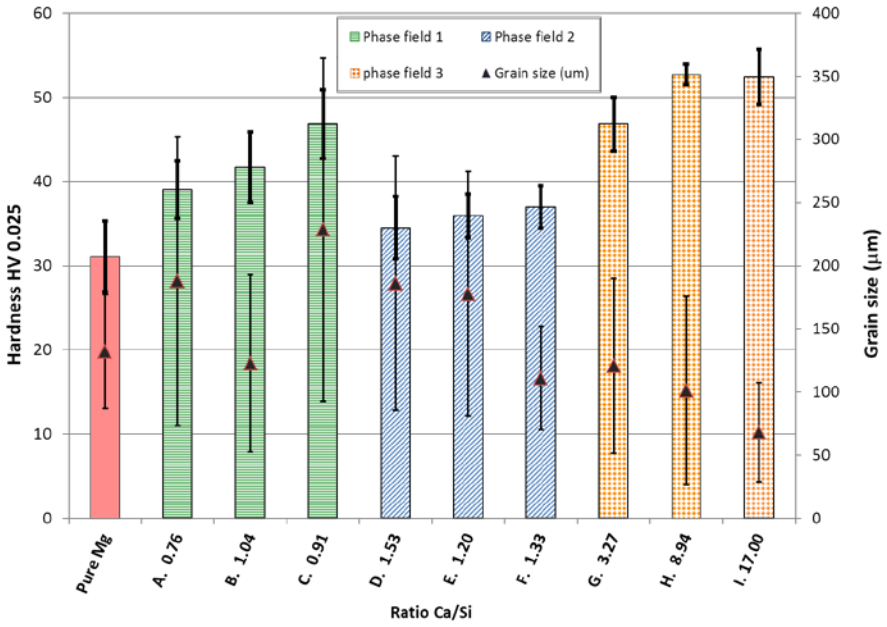

Figure 6. Hardness and grain size values obtained for the as cast Mg-Ca-Si alloys.

For the alloys in the first phase field, it's clear that, irrespectively of the grain size, hardness increases with increasing the amount of Mg_2Si and MgCaSi phases. This is consistent with the noticeable above-mentioned hardening effect of Mg_2Si. In particular, the alloy C shows the highest hardness value. On the one hand, it could be due to the higher amount of Mg_2Si particles present in the alloy (2.8 wt.%) compared with the amount in alloys A (0.3 wt.%) or B (1.0 wt.%). This result has been observed before by Gupta et al. [18] and Zhu et al. [19]. Thus, a precipitation hardening effect from the Mg_2Si phase could be the main cause. On the other hand, as it is presented in Table III, the solidification range for MgCaSi is higher in C (27°C) than in B (22°C) or A (7°C), resulting in larger particles in C which contribute more to the hardening effect. The presence of Mg_2Si particles seems to have the most important effect on the mechanical properties, as was also mentioned by Mabuchi et al. [20] for Mg-Si alloys.

In alloys D, E and F in phase field 2, the hardness increases with decreasing both the amount of MgCaSi particles and the grain size. This means that, despite the MgCaSi particles have a positive

effect on hardness (even those alloys with larger grain size are harder than pure Mg), the mechanical behaviour of these alloys are mainly determined by the grain size.

It can be observed that the alloys in phase field 3, where the Mg, Mg_2Ca and MgCaSi phases coexist, present higher hardness values compared to those observed for the other two phase fields. This observation is consistent with the noticeable above-mentioned hardening effect of Mg_2Ca. Nevertheless it is difficult to determine if this hardening effect of Mg_2Ca is higher than that of Mg_2Si because the grain size of the alloys in phase field 3 is very low, which also results in an increase of the hardness.

The compression results presented in Figure 7 can also be related with the alloy microstructures.

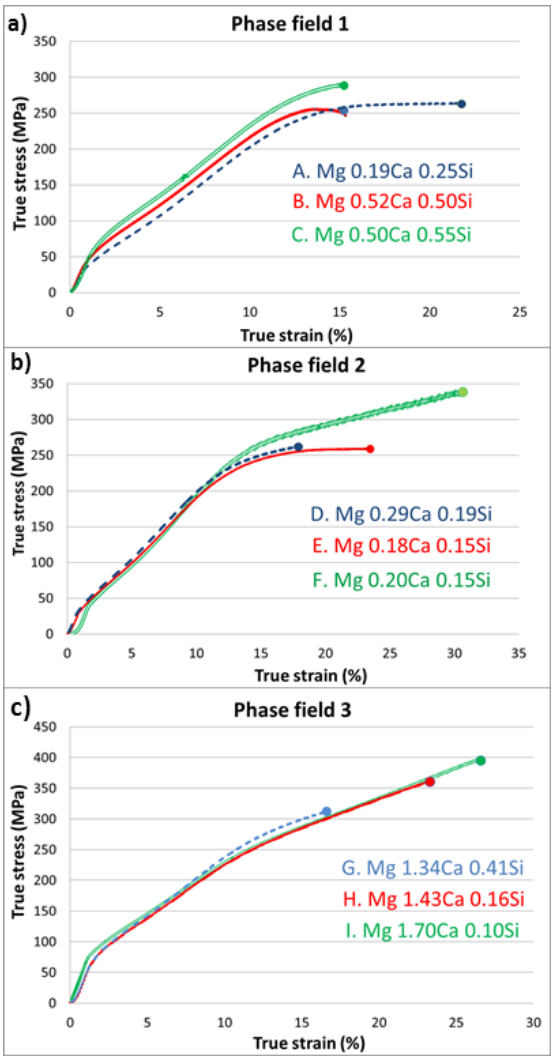

Figure 7. Compressive strength curves (true stress vs true strain) for the different compositions within the phase fields named 1, 2 and 3 in the Mg-Ca-Si system.

When considering the results from compression tests in phase field 1, as plotted in Figure 7a and summarized in Table IV, it can be seen that alloy A with a smaller amount of alloying elements and thus less intermetallic phases has a lower compressive strength and higher ductility. Alloys B and C have a similar alloy element percentage, but C has a higher amount of intermetallic phases, giving it the highest compressive strength. When analysing the influence of the Mg_2Si, it is observed that the

specimens with higher amounts of the binary compound have higher values of compressive strength and low values for ductility (down to half of the value obtained for pure Mg) indicating an embrittling effect of the phase in the alloys. Mg_2Si has an anti-fluorite type structure [21] with a face-centred cubic (fcc) crystal symmetry. Takeuchi et al. [22] studied the plastic deformation behaviour of the phase and showed that the crystals were brittle below 500K. Mg_2Si has been demonstrated to be a rigid phase, based on first-principles calculations by Benhai et al. [23]. The low ductility characteristic effect on the phase is then the expected one at room temperature.

Compression test results obtained for alloys in phase field 2 are plotted in Figure 7b and summarized in Table IV. In this field, some conclusions about the influence of the MgCaSi ternary phase on the alloy ductility can be obtained. The Mg matrix only contains the finer MgCaSi phase and its influence can be analyzed independently from that of other intermetallics. It can be observed experimentally (Table IV) that when the amount of the ternary phase increases the ductility of the alloys is reduced. In this sense, the presence of the MgCaSi phase embrittles the alloys. A trend in the compressive strength is not clear from the results, but when the alloys are compared with pure Mg the effect of the MgCaSi phase is evident, as it increases the compressive strength.

The compression curves obtained for the alloys in phase field 3 are plotted in Figure 7c and summarized in Table IV. The presence of Mg_2Ca phase in this field results in the highest compressive strength values when compared to the rest of the alloys. The ductility of the alloys is higher in alloys H and I than in G, where the presence of the Mg_2Ca phase is also higher. This can be related to the crystalline structure of the Mg_2Ca laves phase, which has a HCP-P63 mmc structure [21], for which it has been theoretically demonstrated based on first principles calculations by Mao et al. [24] that it is a ductil phase.

Table IV. Experimental phase fraction values of the intermetallic phases (wt.%) for all the alloys and their compressive strength, elongation values and grain size.

Group	Sample composition (wt.%)	Exp.wt.% of Mg_2Ca	Exp.wt.% of MgCaSi	Exp.wt.% of Mg_2Si	Compressive strength MPa (0.2% compression)	%Strain at ultimate Comp. strength	Grain size (μm)
1	**A. Mg 0.19Ca 0.25Si**		0.2	0.3	45.5 ± 1.3	21.9 ± 3.2	118 ± 114
	B. Mg 0.52Ca 0.50Si		0.6	1.0	65.3 ± 5.5	15.9 ± 1.1	123 ± 70
	C. Mg 0.50Ca 0.55Si		1.2	2.8	68.1 ± 1.6	16.0 ± 0.2	229 ± 136
2	**D. Mg 0.29Ca 0.19Si**		2.3		45.3 ± 1.1	18.0 ± 3.4	186 ± 101
	E. Mg 0.18Ca 0.15Si		1.6		42.7 ± 1.3	23.5 ± 2.5	171 ± 92
	F. Mg0.20Ca 0.15Si		0.9		49.1 ± 1.6	30.4 ± 3.1	111 ± 41
3	**G. Mg 1.34Ca 0.41Si**	0.8	2.8		74.1 ± 1.4	16.6 ± 1.6	121 ± 69
	H. Mg 1.43Ca 0.16Si	4.4	0.6		70.9 ± 4.6	23.3 ± 3.2	101 ± 75
	I. Mg 1.70Ca 0.10Si	3.9	0.4		84.0 ± 0.9	26.6 ± 0.1	68 ± 40
	Pure Mg				24.2 ± 1.5	33.4 ± 2.6	132 ± 45

4. Summary

Three different phase fields have been predicted based on thermodynamic calculations and experimentally verified in the Mg rich corner of the ternary Mg-Ca-Si diagram. Based on the predictions, compositions with a wt.%Ca:wt.%Si ratio below 1.4 are in the phase field 1 (Mg + Mg_2Si + MgCaSi), ratios between 1.4 and 1.7 limit the phase field 2 (Mg + MgCaSi) and in phase field 3 (Mg + Mg_2Ca + MgCaSi) wt.%Ca:wt.%Si ratio is bigger than 1.7.

The Mg-Ca-Si employed database (TCMG2 from Thermo-Calc software) has been tested by comparison the predictions with the experimental results concluding that it constitutes a worthy tool in microstructure prediction.

The alloys as-cast microstructures have been related with their solidification process, focusing on the formation of intermetallic phases. The influence of the intermetallics on the mechanical performance has been analyzed as well.

In the phase field 1, MgCaSi presents different morphologies, from coarse particles to small needle like ones. Bigger size and higher amounts of the intermetallic phase softly increase the alloys strength and make them brittle. The Mg_2Si phase appears in its needle-like small size morphology and it mainly contributes to an increase of the hardness and compressive strength. Its presence reduces the alloy's ductility.

In the phase field 2, the ternary phase solidifies almost simultaneously with the Mg phase. Grain size reduction is related with a low increase of the hardness and decrease of ductility while the MgCaSi phase seems to have a minor effect on the alloys mechanical response. When the amount of MgCaSi phase increases it accumulates inside the grains and not in grain boundaries favouring its more homogeneous distribution.

In the phase field 3, the Mg_2Ca binary phase is present in a interdendritic structure and the MgCaSi ternary phase presents, like in phase field 1, its two morphologies. The alloys within this field show the highest values for compressive strength and hardness, due to the Mg_2Ca presence. If combined with a low amount of finely distributed MgCaSi (not polygonal shaped morphology), the alloys have elevated ductility values as well. The Mg_2Ca phase accumulates at grain boundaries increasing their amount when the amount of Mg_2Ca increases. This phase has then a grain refining effect.

Acknowledgements

The research was supported by the PEOPLE programme (Marie Sklodowska-Curie Action) of the EU FP7 Programme FP7/ 2007-2013/ under REA grant agreement n°289163. The authors are personally grateful to Meritxell Ruiz, Rocio Munoz and Thomas Lapauw for their help on proofreading of the manuscript.

References

1. Witte, F., *The history of biodegradable magnesium implants: a review.* Acta biomaterialia, 2010. **6**(5): p. 1680-1692.

2. Zheng, Y.F., X.N. Gu, and F. Witte, *Biodegradable metals.* Materials Science and Engineering: R: Reports, 2014. **77**: p. 1-34.
3. Bakhsheshi-Rad, H.R., et al., *Mechanical and bio-corrosion properties of quaternary Mg–Ca–Mn–Zn alloys compared with binary Mg–Ca alloys.* Materials & Design, 2014. **53**: p. 283-292.
4. T.D.Luckey, B.V., *Metal toxicity in mammals* Vol. 1. 1977, New York
5. Carlisle, E.M., *Silicon: A Possible Factor in Bone Calcification.* Science, 1970. **167**(3916): p. 279-280.
6. Carlisle, E.M., *Silicon as an Essential Trace Element in Animal Nutrition*, in *Ciba Foundation Symposium 121 - Silicon Biochemistry*2007, John Wiley & Sons, Ltd. p. 123-139.
7. G.V.Raynor, *The physical metallurgy of magnesium and its alloys*1959, London: Pergamon Press LTD.
8. H. E. Friedrich, B.L.M., *Metallurgy, Design Data, Applications*, in *Magnesium Technology*2006, Springer-Verlag Berlin Heidelberg. p. 122-124.
9. Carbonneau, Y., et al., *On the observation of a new ternary MgSiCa phase in Mg-Si alloys.* Metallurgical and Materials Transactions A, 1998. **29**(6): p. 1759-1763.
10. Yanling, A., et al., *As-Cast Microstructure and its Formation Mechanism in Mg-Based Alloys Containing Ca And Si.* Acta Metall, 2005. **41**(1): p. 49.
11. Ai, Y., C.P. Luo, and J. Liu, *Twinning of CaMgSi phase in a cast Mg–1.0Ca–0.5Si–0.3Zr alloy.* Acta Materialia, 2007. **55**(2): p. 531-538.
12. International, A., *Standard Test Methods for Determining Average Grain Size*, in *E112 - 13*2013.
13. Andersson, J.O., et al., *Thermo-Calc & DICTRA, computational tools for materials science.* Calphad, 2002. **26**(2): p. 273-312.
14. *Thermo-Calc software User's guide "Examples of solidification simulation using TCMG3"* 2014.
15. Scheil, E., *Bemerkungen zur schichtkristallbildung.* Z. Metallk, 1942. **37**: p. 70-72.
16. Gulliver, G., *The quantitative effect of rapid cooling upon the constitution of binary alloys.* The Journal of the Institute of Metals, 1913. **9**: p. 120.
17. Schmid-Fetzer, R., *Phase Diagrams: The Beginning of Wisdom.* Journal of Phase Equilibria and Diffusion, 2014. **35**(6): p. 735-760.
18. Gupta, A.K., D.J. Lloyd, and S.A. Court, *Precipitation hardening in Al–Mg–Si alloys with and without excess Si.* Materials Science and Engineering: A, 2001. **316**(1–2): p. 11-17.
19. Zhu, Z. and M.J. Starink, *Solution strengthening and age hardening capability of Al–Mg–Mn alloys with small additions of Cu.* Materials Science and Engineering: A, 2008. **488**(1–2): p. 125-133.
20. Mabuchi, M., K. Kubota, and K. Higashi, *Tensile strength, ductility and fracture of magnesium-silicon alloys.* Journal of Materials Science, 1996. **31**(6): p. 1529-1535.
21. *Crystallography Open Database* Available from: http://www.crystallography.net/.
22. Zhang, J. and Z. Fan, *Microstructure and mechanical properties of in situ Al–Mg2Si composites.* Materials science and technology, 2000. **16**(7-8): p. 913-918.
23. Yu, B., et al., *Structural, electronic, elastic and thermal properties of Mg2Si.* Journal of Physics and Chemistry of Solids, 2010. **71**(5): p. 758-763.
24. Mao, P.-l., et al., *Mechanical properties and electronic structures of MgCu 2, Mg 2 Ca and MgZn 2 Laves phases by first principles calculations.* Transactions of Nonferrous Metals Society of China, 2014. **24**(9): p. 2920-2929.